Quantification of charge compensation in lithium- and manganese-rich Li-ion cathode materials by x-ray spectroscopies

Shehab E. Ali [a,b], Wojciech Olszewski [a,c], Carlo Marini [a], Arefeh Kazzazi [d,e], Hyeongseon Choi [d,e], Matthias Kuenzel [d,e], Dominic Bresser [d,e], Stefano Passerini [d,e], Dino Tonti [f,**], Laura Simonelli [a,*]

[a] ALBA Synchrotron Light Facility, Carrer de la Llum 2-26, 08290, Cerdanyola del Vallès, Spain
[b] Physics Department, Faculty of Science, Suez Canal University, Ismailia, Egypt
[c] Faculty of Physics, University of Bialystok, ul. K. Ciolkowskiego 1L, 15-245, Bialystok, Poland
[d] Helmholtz Institute Ulm (HIU), Helmholtzstrasse 11, 89081, Ulm, Germany
[e] Karlsruhe Institute of Technology (KIT), PO Box 3640, 76021, Karlsruhe, Germany
[f] Institut de Ciència de Materials de Barcelona (ICMAB), CSIC, Campus UAB Bellaterra, Spain

A B S T R A C T

The reversible and irreversible cationic and anionic charge compensation mechanisms occurring along the first charge and discharge cycle of Li- and Mn-rich Li [Li$_{0.2}$Ni$_{0.16}$Mn$_{0.56}$Co$_{0.08}$]O$_2$ cathode material at (dis)charge rates of 0.1C and 5C have been identified and quantified by X-ray absorption and emission spectroscopy. The analysis provided the oxidation states of the transition metals, the Mn local coordination, and the lattice elastic constants. Lattice softening occurs along the first charge, while a minor spinel phase forms irreversibly at the expense of the layered phase. Higher charge rate increases the spinel formation and induces an increased softening in the delithiated lattice, which is expected to correspond to a reduced reversible anionic redox. The results evidence a comparable cationic and anionic oxidation since the beginning of the charge, while only anions are contributing towards its end, equivalent to roughly 10% of structural oxygen irreversibly lost. Higher charge rates resulted in a decreased reversible anionic redox, anticipating the cationic oxidation.

The reported results provide a reliable experimental approach to characterize the key parameters controlling the reversible and irreversible cationic and anionic contributions to the charge compensation mechanism.

1. Introduction

Increasing the contribution of renewable energy sources is necessary to meet the fast increase of global energy needs and match the CO$_2$ reduction targets [1–3]. In order to address these challenges, intensive research efforts are ongoing both in energy harvesting and storage technologies such as solar panels, fuel cells, supercapacitors and batteries [4–7]. The latter are required to match the energy demand and supply; in fact, batteries are by far the most ubiquitous energy storage technology currently employed [8].

Despite the relative scarcity of lithium and other raw materials, Li-ion batteries (LIBs) are cost-effective and affordable offering superior energy and power performance as well as a good cycle life, while being relatively safe [9–11]. As a result, LIBs are currently employed in portable electronics, power tools, stationary storage and, increasingly, electric vehicles [12,13]. Such a widespread use is keeping LIBs in the focus of extensive investigation. LiCoO$_2$ has long been the most exploited cathode in commercial Li-ion batteries [14,15], but is providing a rather low practical capacity (maximum achievable 140 mAh g^{-1}) [7] and relatively high cost associated to the criticality of cobalt [10,16]. The need for reducing cost and increasing energy density pushed to partially substitute Co with other transition metals, i.e., Mn and Ni, leading to the well-established LiNi$_x$Mn$_y$Co$_z$O$_2$ (NMC$_{xyz}$) cathodes with specific capacities over 200 mAh g^{-1} at elevated Ni contents (x > 0.8) [17]. However, the increasing Ni content also introduces new challenges, such as the pronounced sensitivity of the material towards water leading to difficulties during electrode preparation which requires strictly controlled atmosphere. Moreover, safety risks exist due to the lower thermal stability of Ni-rich materials (e.g., NMC$_{811}$) [18,19]. Therefore, a newer class of Li-rich layered oxides (LR-NMC), where part of the transition metals is substituted by Li, are in the focus as a very promising alternative due to the very low Ni and Co content as well the significantly higher energy density, theoretically reaching 1000 Wh kg^{-1} with respect to the cathode active material [1,7].

The high specific capacity of LR-NMC, exceeding 250 mAh g^{-1}, originates from the contribution of the anionic redox activity [20–22], i.

* Corresponding author.
** Corresponding author.
E-mail addresses: dino.t@csic.es (D. Tonti), lsimonelli@cells.es (L. Simonelli).

e., the partial oxidation of the oxide anions upon additional Li extraction from the transition metal layer, accompanied by a partial irreversible capacity loss especially pronounced during the first cycle [23–26]. The electronic and structural reasons for this irreversibility have been intensively investigated in the past years. Generally, it is accepted that during the initial delithiation LR-NMC crystals undergo a structural transformation involving the cation migration from the transition metal (TM) layer into the lithium layer. This results in the formation of antisite TM cation-vacancy (V) defect pairs (TM_{Li}-V_{TM}). The reversibility of the TM migration has a crucial impact on the capacity and voltage fading of LR-NMC [5,27,28]. Particularly, it was shown that the structural and electronic properties of $Li[Li_{0.2}Ni_{0.16}Mn_{0.56}Co_{0.08}]O_2$ are substantially affected by the electrochemical de-/intercalation of lithium cations [20, 21,29], having a direct impact on the formation of different local phases [22]. During the first charge, an irreversible spinel-like reconstruction layer occurs at the expenses of the pristine Li-rich layered phase [30]. Along the first charge, the out-of-plane cation migration [27,31–33] appears to correlate with the phase transition from the layered to the spinel-like phase [28,34–37] and the oxygen oxidation [22,29], potentially accompanied by irreversible O_2 release. Moreover, it has been recently proposed that a larger degree of overlap between the transition metal and oxygen electronic states introduces a more rigid oxygen sublattice upon lithium deintercalation and results in a more reversible oxygen redox [38]. All these parameters are considered to affect the cycling and voltage stability of LR-NMC and need to be considered for design guidelines for novel high-energy positive electrode materials.

The increase of the dis-/charge rate, which is key for the practical application in, e.g., electric vehicles, is expected to affect the ion diffusion and local strains. Indeed, ion kinetics variations can alter the local equilibrium in between coexisting phases along the active material and during the charge compensation, also affecting local strains. The key role of such strains in governing the competing Mn phases (spinel and layered) in Li- and Mn-rich NMC cathodes has been very recently highlighted [22]. In particular, the local strains induced by the Ni oxidation have been found to induce the formation of a low spin (LS) Mn^{3+} in the layered structure in parallel to the irreversible formation of the spinel phase in the bulk particles. The charge balance, affected by the partial Mn reduction, requires a certain reversible fraction of oxygen oxidation along the charge, enabling the outstanding cathode capacity. From one other point of view, different oxide local phases show different degrees of metal and oxygen density of states (DOS) overlap near the Fermi level. A lower DOS overlap is expected to correspond to a higher tendency to form O–O dimers within the octahedron due to less-directional M−O bonding and lower lattice stiffness, favoring a higher irreversible oxygen oxidation fraction [38].

Here, we report the investigation of the local structural and electronic properties of $Li[Li_{0.2}Ni_{0.16}Mn_{0.56}Co_{0.08}]O_2$ at different states of charge and for different charge rates. Temperature-dependent Mn, Co and Ni K-edge X-ray absorption spectra have been acquired to access quantitatively the spinel phase formation and local bond characteristics in terms of local strains, lattice rigidity and structural disorder, which are expected to directly correlate with the electrochemical behavior [22, 38–40]. In particular, the temperature-dependent investigation revealed experimentally the evolution of the lattice rigidity which directly affects the reversible anionic redox contribution [38]. Finally, the combination of the absorption measurements and room temperature Mn Kβ X-ray emission spectroscopy results allowed to fully characterize the charge transfer mechanism, including quantitative determination of the O oxidation along the first charge.

2. Experimental METHODS

2.1. Material synthesis and electrode preparation

The $Li[Li_{0.2}Ni_{0.16}Mn_{0.56}Co_{0.08}]O_2$ samples were synthetized by co-precipitation, followed by a solid-state reaction, using the transition metal acetates and $LiOH·H_2O$ as precursors [41]. The electrode composition was 85 wt% LR-NMC, 10 wt% conductive carbon (C-NERGY Super C45, Imerys) and 5 wt% carboxymethyl cellulose (CMC; Dow Wolff Cellulosics, Walocel CRT 2000). To prepare the electrodes, CMC was first dissolved in deionized H_2O. Next, the active material and the conductive carbon were dispersed in the CMC-based solution by planetary ball milling (Pulverisette 4, Fritsch) for 3 h. Finally, the resulting slurry was coated on Al foil using a doctor blade method. The resulting electrode sheets were dried at 60 °C for 10 min and at room temperature in the dry room (dew point <70 °C) overnight. Disk-shaped electrodes with a diameter of 12 mm were punched out of the electrode sheets, pressed at 4 t cm^{-2}, and dried at 180 °C under vacuum for 14 h. The active material mass loading was around 3.1 mg cm^{-2} [42].

2.2. Electrochemical characterization and sample preparation

The electrodes were cycled in two-electrode pouch-type cells with lithium metal foil (Honjo, battery grade) serving as counter electrode. The cells were assembled in the dry room (dew point <70 °C). Whatman glass fiber sheets (GF/A) served as the separator and were drenched with 100 μL of the electrolyte (1 M $LiPF_6$ in a 1:1 wt mixture of ethylene carbonate and dimethyl carbonate; UBE). The galvanostatic cycling was conducted using a battery tester (Maccor 4300), setting the anodic and cathodic cut-off potentials to 4.8 and 2.5 V, respectively. The dis-/charge rate of 1C corresponds to a specific current of 200 mA g^{-1}. The cells were stopped at selected states of charge, i.e., the pristine state (P01), the beginning (P03, charge to 100 mAh g^{-1}) and the end (P04, charge to 200 mAh g^{-1}) of the high-voltage plateau, and the fully charged state (P05) as well as the subsequently discharged state (P08, see Fig. 1a), both obtained at the cut-off potentials. Subsequently, the cells were disassembled in an argon-filled glove box. In order to minimize the contribution of the conducting salt or other possible soluble species from the electrolyte, the samples were rinsed with dimethyl carbonate (UBE) and the active material was recovered from the electrodes.

2.3. Hard X-ray absorption and emission measurements

Mn, Co, and Ni K-edge X-ray absorption spectroscopy (XAS) and Mn Kβ emission spectroscopy (XES) were performed at the CLÆSS beamline of the ALBA synchrotron (Spain) [43]. For the XAS measurements, the synchrotron radiation emitted by a wiggler source was monochromatized using a double crystal Si(111) monochromator. Higher harmonics' rejection was done by choosing proper angles and coatings of the collimating and focusing mirrors. The electrodes were mounted into a liquid nitrogen cryostat, and the spectra were recorded in transmission mode at different temperatures from 80 to 300 K (within an accuracy of 1 K) by means of two ionization chambers. X-ray absorption spectra were treated using the Demeter package [44], involving a standard procedure based on the cubic spline fit to the pre-edge subtracted absorption spectra to extract the extended X-ray absorption fine structure (EXAFS) signal [45].

XES data were collected in backscattering geometry by means of the CLEAR emission spectrometer. The spectrometer is based on a diced Si (333) analyzer crystal (bending radius R = 1 m) and a 1D position-sensitive Mythen detector. The emission spectra were acquired by exciting the sample well above the Mn K-edge, monochromatizing the incoming beam with the Si(311) double crystal monochromator, and detecting the emitted Mn Kβ emission lines with a total energy resolution around 0.5 eV. The XES measurements were performed at ambient temperature under vacuum. Similarly to previous reports [20], μ_{Mn} corresponding to the sample set have been extracted from the integrated area of absolute difference (IAD) with respect to a reference. [46] MnO, Mn_2O_3, and MnO_2 were used as references for known μ_{Mn} [47–50]. Several X-ray absorption and emission scans were measured to ensure
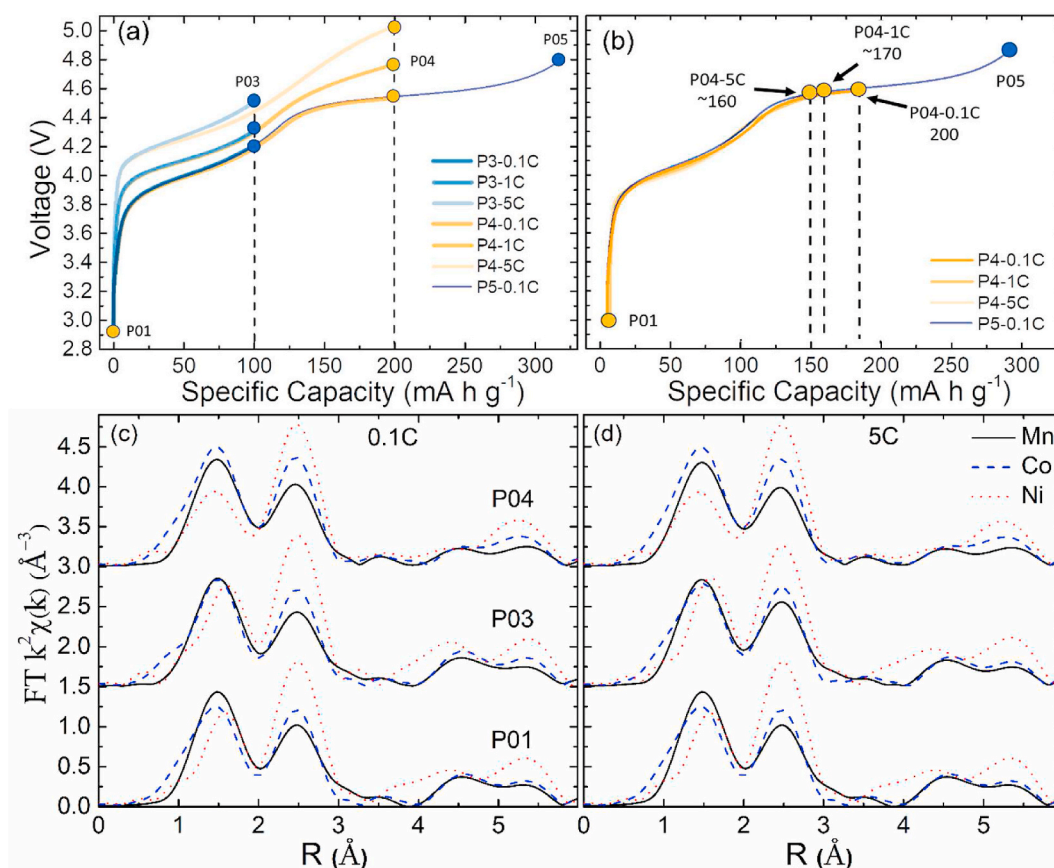
Fig. 1. (a) Voltage profiles of Li[Li$_{0.2}$Ni$_{0.16}$Mn$_{0.56}$Co$_{0.08}$]O$_2$ cathodes in half-cell configuration, where the different cut-off points P01 (pristine), P03 and P04 (beginning and end of the voltage plateau), and P05 (fully charged) are indicated. (b) The same voltage profiles being corrected taking into account the current-induced overpotential and possible side reactions. (c,d) Magnitudes of the Fourier transforms (FTs) of the EXAFS signal at the Mn, Co, and Ni K-edge collected at 80 K of the Li[Li$_{0.2}$Ni$_{0.16}$Mn$_{0.56}$Co$_{0.08}$]O$_2$ samples P01 (pristine), P03 and P04 (beginning and end of the voltage plateau) cycled at (c) 0.1C and (d) 5C.

the reproducibility of the spectra and to obtain high signal-to-noise-ratio.

3. Results and DISCUSSION

The Li[Li$_{0.2}$Ni$_{0.16}$Mn$_{0.56}$Co$_{0.08}$]O$_2$ cathode voltage profiles obtained at different charge rates (0.1C, 1C and 5C) are reported in Fig. 1a, together with the labeling of the charge points investigated herein. Fig. 1b depicts the same voltage profiles, normalized by the current-induced overpotential in order to estimate the capacity contribution from side reactions with the electrolyte at elevated potentials (details are provided in the Supporting Information). The approximation made does not consider that high charge rates, besides accelerating side reactions due to the relatively higher overpotential, could also alter the oxidation path, with possibly different structural evolution, as we indeed observed within this study. However, the good empirical matching of the normalized curves shown in Fig. 1b and Fig. S1 indicates that the assumption is sufficiently accurate for the given purpose. Temperature-dependent EXAFS at the Mn, Co, and Ni K-edges have been measured for the electrodes charged at 0.1C and 5C. The corresponding magnitude of the Fourier transforms (FTs) of the EXAFS signal collected at 80 K are shown in Fig. 1c and d. The FT main peaks at ~1.5 Å and ~2.4 Å correspond to single scattering contributions from the first and second coordination shell around the photo-absorbing atom (TM), composed of O and TM (TM = Mn, Co, Ni) atoms, respectively. The charge rate turns out to have generally a weak effect on the EXAFS oscillations, i.e. the FTs, highlighting no major effects on the global local structural properties. Upon charge the Ni–O bond length substantially shortens and its distribution becomes broader compared to Mn–O and

Co–O bonds, which implies a more disordered configuration. The second-shell FT peak is more stable during the charge process, but as it corresponds to different contributions, compensating variations cannot be excluded. The absorption spectra were modeled considering a partial structural degradation of the layered phase into a spinel phase as a function of charge, as reported in the literature [21,22,26]. Particular attention has been put in keeping the number of free fitting parameters always below the intrinsic limit defined by the Nyquist theorem [45] and the data quality. The full details of the EXAFS data modeling are reported in the Supporting Information. The fitting results allow to follow the evolution of the Mn layered and spinel phase ratio, as well as the Co^{4+} and Ni^{4+} formation as a function of the charge point, as shown in Fig. 2a and Fig. 2b, respectively. While the Mn layered and spinel ratio has been obtained by modelling the EXAFS oscillations with a combination of the two structural phases, the Ni and Co oxidation states have been determined indirectly from the Ni–O and Co–O bond distances.

Fig. 2a indicates that the strong increase of the charge rate from 0.1C to 5C accelerates the spinel phase formation, presumably at the expense of cycling stability. Indeed, the Jahn−Teller active high spin (HS) Mn^{3+} electronic phase, coexisting with the Mn^{4+} HS phase in the spinel LiMn$_2$O$_4$ (Mn$^{3.5+}$), has been correlated to the capacity loss due to the Jahn−Teller distortion destabilizing the structure upon electrochemical cycling [51–53]. Moreover, a higher charge rate anticipates Co and Ni oxidation (Fig. 2b). This suggests that the Li kinetics, directly affected by the charge rate, influence the response of the different TM atomic centers, acting on the local charge compensation mechanism and induced strains.

Even if generally XAS studies on battery materials are performed at a single temperature to access the charge transfer mechanisms and
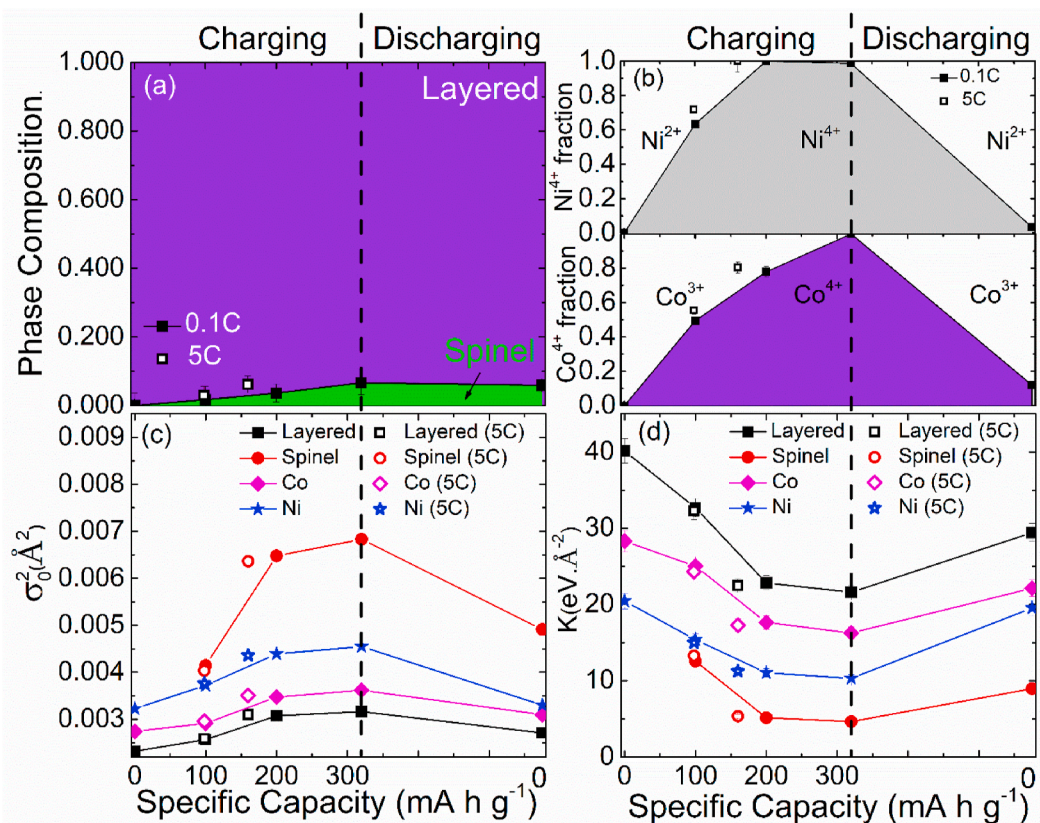
Fig. 2. (a) Estimation of the layered/spinel phase ratio evolution and the (b) change in cation oxidation state fractions, Ni^{4+} vs Ni^{2+} (upper panel) and Co^{4+} vs Co^{3+} (lower panel), as a function of capacity along the first charge. (c) Low temperature Debye-Waller factor (DWF; σ_0 [2]) and (d) local force constants (K) for the Mn–O bond in both layered and spinel phases as well as for the Co–O bond and Ni–O bond as a function of capacity. The filled symbols represent 0.1C, while the open symbols 5C charging rate.

structural evolutions along the cycling, ex-situ temperature dependent measurements provide additional information on the local structure affecting the battery performance. Details on the Mn–O, Co–O, and Ni–O interatomic distances (R) and their corresponding mean square relative displacements (MSRDs) (σ^2) have been provided by fitting the Mn, Co, and Ni K-edge EXAFS spectra collected as a function of temperature, as shown in Fig. S3 and Fig. S4 for the Mn layered and Mn spinel structure, respectively. The results agree with those reported in the literature regarding the contraction of the Co–O, and Ni–O distances by charging [21,22], while the forming spinel Mn–O bond shows a significantly larger distance, accordingly to its bulk structure [22]. This further confirms that while Co and Ni are oxidized, there is an effective Mn reduction [24] during the first charge.

The temperature effect on the local bond distances and on the σ_i [2] permits accessing the rigidity of the lattice. The local bond thermal contraction (Fig. S3) tends to increase from the pristine to the charged state, and from the layered to the spinel phase. This suggests a global softening of the lattice upon charge, as also confirmed by the following findings. Indeed, the quantitative direct access to the local force bond, i. e., the lattice stiffness, is provided by the Einstein model, describing the temperature evolution of σ_i [2], σ_i [2] $= \sigma_0$ [2] $+ \sigma^2$ (T), where σ_0 [2], extrapolated for T = 0 K, corresponds to the static structural disorder [38]. The Einstein frequency ($\omega_E = k_B\theta_E/\hbar$) and the effective local force constant (K $= \mu \, \omega_E^2$) have been calculated for the Mn–O, Co–O, and Ni–O atomic pairs. Details are reported in the supplementary information. The static disorder σ_0 [2] and the local force constant K obtained for the different atomic pairs are presented in Fig. 2c and d, respectively. While all σ_0 [2] values increase, consistent with the occurrence of coexisting phases and induced strains [20,22], all K values decrease upon charge, indicating the softening of the lattice, which is expected to favor the ion

diffusion [39,40]. From one other point of view, it has been demonstrated that the electronic structure is coupled with the rigidity of structure upon lithium deintercalation, where a larger degree of energetic overlap between the TM and oxygen induces a more rigid oxygen lattice and the reversibility of anionic redox scales with the degree of overlap between the TM d and O 2p states [38].

The increase of the charge rate seems to anticipate the lattice softening, mainly along the voltage plateau, where Mn gets activated and the spinel phase mainly forms [22]. The increase in the lattice softening by increasing the charging rate suggest the increase of irreversible anionic redox. The role of oxygen in the charge compensation mechanism becomes accessible by combining the quantification of the spinel phase formation and the Ni and Co oxidation state evolution, shown above, with the local Mn magnetic moment (μ_{Mn}) obtained by XES. This latter allows for extracting the amount of Mn^{3+} in LS configurations, forming in the layered phase during the charge process [20], and probably accompanied by the trapping of O_2 in the lattice [22,29]. Fig. 3a shows selected Mn $K\beta$ emission spectra, while Fig. 3b shows the obtained Mn local magnetic moments. The inset in Fig. 3a shows a zoom over the $K\beta_{1,3}$ main emission line. The energy position of the $K\beta_{1,3}$ feature is as well related to the spin state, reflecting the effective number of unpaired 3d electrons [54]. The $K\beta_{1,3}$ energy positions (Fig. 3c) globally confirm the evolution of the local Mn magnetic moment along the charge, anyway its precise identification is made difficult by the coexisting Mn electronic phases. Upon the initial delithiation, μ_{Mn} drops significantly in a partially irreversible manner (Fig. 3b). This evolution corresponds to an increase of the Mn^{3+} fraction forming in the layered phase along the first charge. The increase in charge rate affects the Mn^{3+} LS formation, most likely because of a difference in local strains. Prior to the voltage plateau (P01 to P03, 0 → 100 mAh g^{-1}) this behavior seems
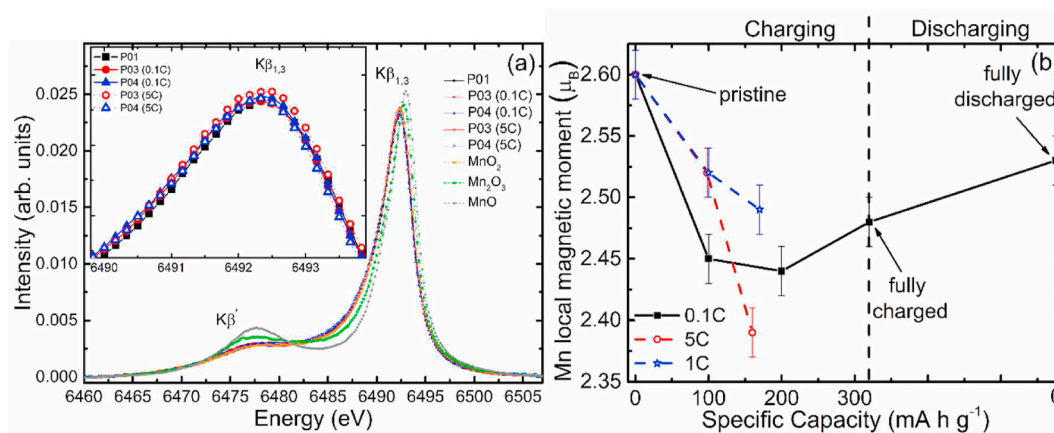
Fig. 3. (a) Mn Kβ emission line for Li[Li$_{0.2}$Ni$_{0.16}$Mn$_{0.56}$Co$_{0.08}$]O$_2$ samples, compared with the MnO$_2$, Mn$_2$O$_3$ and MnO references. (b) Evolution of the extracted Mn local magnetic moment as a function of the specific capacity and charging/discharging rate, 0.1C (filled black squares), 5C (unfilled red circles), and 1C (unfilled blue stars).

to slow down with an increasing charge rate, with 1C and 5C providing similar results. Along the voltage plateau (P03 to P04, 100 → 200 mAh g^{-1}), while 1C charging seems to slower the Mn^{3+} LS formation, 5C charging is favoring it, probably because of different kinetics. The total spinel formation (Fig. 2a) and its local strains affecting the Mn–O bond distance (Fig. S3) could be at the origin of such different amount of Mn^{3+} LS phase formation, with a compressed Mn–O spinel network which seems to slow down the formation of this phase.

By considering the average Mn local magnetic moment together with the spinel phase formation, the relative fraction of the three Mn electronic configurations (Mn^{3+} HS, Mn^{3+} LS, Mn^{4+} HS) [47–50] can be quantitatively determined (Fig. 4a). Combining these results with the estimated Ni and Co oxidation states (Fig. 2b), the O oxidation state can now be also quantitatively extracted (Fig. 4b). From the graph it is possible to appreciate how the oxygen progressively oxidizes along the first charge, with faster charge attenuating the phenomena.

Delithiation is driven by the compensation of the electronic charge removed during the charge process. In the case of lithium-rich compounds the electron is considered removed both from transition metals and oxygen, which is known respectively as cationic and anionic charge compensation. The data reported in Figs. 2b and 4a can be used to determine the cationic compensation, and by imposing electroneutrality the anionic component is determined as well. Fig. 5a reports the global anionic and cationic (Mn, Ni, Co) charge vs. the Li content while the

insert represents the same amounts respect to pristine, so that values are directly the variations that occurred to compensate Li$^+$ extraction. In panel b are shown the fractions of anionic and cationic contribution to the global charge compensation mechanism. Interestingly, the two contributions increase in similar amount by delithiation up to P04, while only the anionic contribution is significantly compensating the Li extraction after this point. However, this anionic contribution is known to be partially irreversible and, among others, leads to the release of molecular oxygen especially at the end of the voltage plateau [25,38], when the Li stoichiometry falls below 0.6. The amount of the irreversibly lost structural oxygen can be deduced by the global anionic charge at P08, the subsequent fully discharged state. Indeed, whereas the cationic charge reverts to its initial value, the anionic charge changes from −4 in the pristine (P01) to −3.6 in the first fully discharged point (P08). This difference indicates that up to 10% of oxygen is removed from the lattice. We may note, though, that, in line with other reports, we did not observe a significant amount of gas evolving, i.e., we did not notice any inflation of the pouch cells used for cycling. Therefore, we assume that this oxygen is either dissolved in the electrolyte or reacting with the electrolyte, forming non-volatile oxidized species.

Instead, almost the 50% of the anionic contributions to the charge compensation mechanism is reversible, and it corresponds to the anionic contribution variation between the fully charged and discharged state (inset in Fig. 5a), in agreement with the relatively high cyclability after
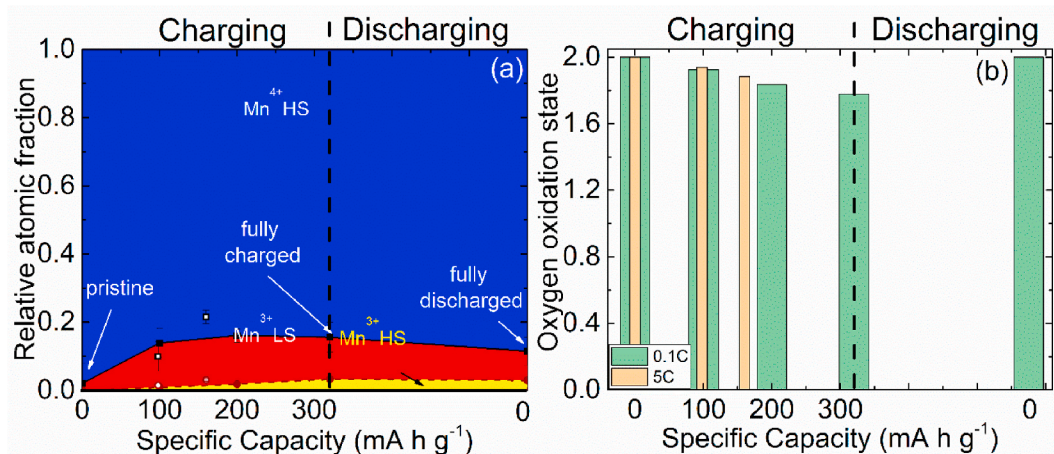

Fig. 4. (a) Quantitative amount of the Mn^{3+} LS/HS and Mn^{4+} HS components for different charge points, estimated by combining the XAS and XES results, closed symbols for 0.1C and open symbols for 5C. (b) Quantification of the corresponding O oxidation state evaluating the Li amount from the capacity corresponding to the different charge state.
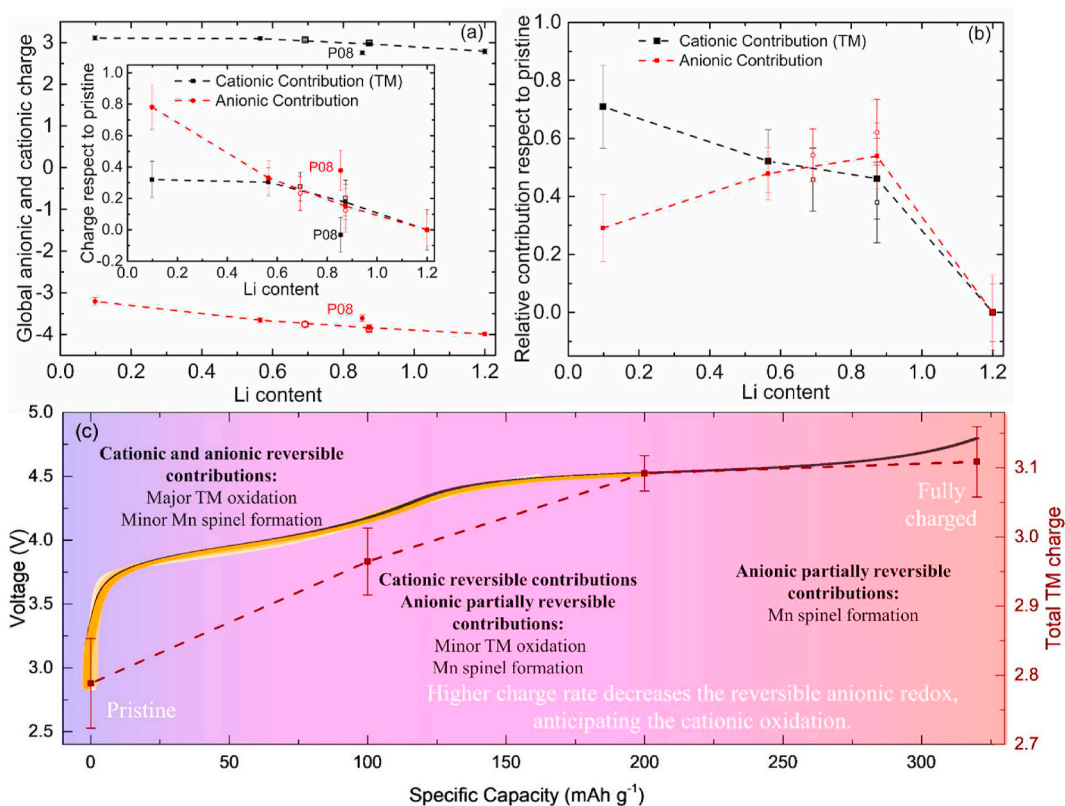
Fig. 5. (a) Extracted global anionic (O) and cationic (TM) charge, where the inset is reporting the charge respect to pristine sample (P01). (b) Fraction of the anionic and cationic contributions to the charge compensation mechanism, calculated as anionic(cationic) contribution/(anionic contribution + cationic contribution). (c) Graphical representation of the main anionic and cationic contributions along the first charge. The full (open) symbols report the values obtained for slow (0.1C) and fast (5C) charge rate.

the first charge [55].

Regarding the cationic contribution to the charge compensation mechanism, the comparison of the fully discharge state (P08) and the pristine (P01) cationic charge shows a slight decrease that can be attributed to the irreversible formation of around 7% of the spinel phase. The rest of the cationic contributions to the charge compensation mechanism is reversible.

Increasing the charge rate from 0.1C to 5C is anticipating the cation oxidation, while decreasing the anion contribution along the voltage plateau. This could be caused by a faster kinetics of the TM oxidation compared to oxygen, probably due to the smaller activation implied by more limited structural rearrangements that take place at these centers. This, together with the detected increase in the lattice softening upon delithiation, suggests a suppression of reversible anionic redox at increased charge rates.

The here reported findings are summarized in Fig. 5c. The total TM charge is directly compared with the voltage curve and the effect of a high rate cycling is summarized. A color gradient represents three main regions. The first one (violet) before the voltage plateau, where Ni and Co are largely oxidized and the spinel phase forms irreversibly to a minor amount. In this first region, the cationic and anionic contributions are comparable and reversible, i.e. cycling does not show a quick capacity lost. The second region (pink) corresponds to the voltage plateau, where Ni and Co are oxidized to a minor extent and almost the half of the total irreversible spinel phase formation occurs. In this second region, while the cationic contribution is almost reversible, the anionic contribution is only partially reversible. The third and last region (red) is toward the end of the voltage plateau, where Ni and Co are inactive andfurther irreversible spinel formation occurs. Also in this region, the anionic contributions are partially irreversible, probably with different mechanisms, since the absence of cationic contributions, instead present

along the voltage plateau.

4. Conclusions

In this work the reversible and irreversible cationic and anionic charge compensations occurring along the first charge and discharge cycle of Li- and Mn-rich $Li[Li_{0.2}Ni_{0.16}Mn_{0.56}Co_{0.08}]O_2$ cathode material have been quantified. The combination of Mn, Ni and Co K-edge absorption and Mn Kβ emission spectroscopies allowed to identify all the local co-existing TM electronic configurations and their evolution along the first cycle. Particularly, in agreement with previous results, around the 7% of a spinel phase forms irreversibly at the expenses of the layered phase. The effect of 0.1C cycling has been compared with faster charge rate. Higher charge rate increases the Mn spinel formation and induce a deeper softening in the delithiated lattice, which is expected to correspond to a less significant anionic reversible redox. Ni and Co redox states have been indirectly quantified by the Ni–O and Co–O local distances, while the Mn redox was determined based on the amount of the spinel phase formation and average local Mn magnetic moment. Combining the characterization of the coexisting chemical phases with the cathode capacity, the global cationic, and corresponding anionic, charge evolution has been quantified. The results evidence a constant comparable cationic and anionic oxidation up to the end of the voltage plateau. While Ni and Co are mainly oxidizing before, the Mn spinel formation occurs mainly along the voltage plateau. At the end of the voltage plateau the cations do not contribute, while the anions are compensating the charge. A total of 10% of irreversible structural oxygen is lost, most likely during and at the end of the voltage plateau. The application of higher charge rates decreases the reversible anionic redox, anticipating the cationic oxidation.

In the past we identified the Ni oxidation as the major cause of strains

in these materials [20,22]. However, the LR-NMC capacity is also strongly affected by the Ni content. Thus, the identification of a good compromise between these two properties seems key to achieve the best performing materials.

Credit author statement

Shehab E. Ali: Formal analysis, Visualization, Writing – original draft **Wojciech Olszewski:** Investigation **Carlo Marini:** Investigation **Arefeh Kazzazi:** Investigation **Hyeongseon Choi:** Investigation **Matthias Kuenzel:** Investigation, Formal analysis, Writing – review & editing **Dominic Bresser:** Methodology, Writing – review & editing, Supervision, Conceptualization **Stefano Passerini** Writing – review & editing, Funding acquisition **Dino Tonti:** Conceptualization, Formal analysis, Writing – review & editing **Laura Simonelli:** Conceptualization, Methodology, Investigation, Formal analysis, Writing – review & editing, Supervision.

Declaration of competing interest

The authors declare that they have no known competing financial interests or personal relationships that could have appeared to influence the work reported in this paper.

Acknowledgement

Appendix A. Supplementary data

Supplementary data to this article can be found online at https://doi.org/10.1016/j.mtphys.2022.100687.

References

[1] N.L. Panwar, S.C. Kaushik, S. Kothari, Role of renewable energy sources in environmental protection: a review, Renew. Sustain. Energy Rev. 15 (3) (2011) 1513–1524.

[2] O. Ellabban, H. Abu-Rub, F. Blaabjerg, Renewable energy resources: current status, future prospects and their enabling technology, Renew. Sustain. Energy Rev. 39 (2014) 748–764.

[3] P.A. Owusu, S. Asumadu-Sarkodie, A review of renewable energy sources, sustainability issues and climate change mitigation, Cogent Eng. 3 (1) (2016) 1167990.

[4] M. Winter, R.J. Brodd, What are batteries, fuel cells, and supercapacitors? Chem. Rev. 104 (10) (2004) 4245–4270.

[5] J.M. Tarascon, M. Armand, Issues and challenges facing rechargeable lithium batteries, Nature 414 (2001) 359.

[6] X. Zeng, M. Li, D. Abd El-Hady, W. Alshitari, A.S. Al-Bogami, J. Lu, K. Amine, Commercialization of lithium battery technologies for electric vehicles, Adv. Energy Mater. 9 (27) (2019) 1900161.

[7] P. Rozier, J.M. Tarascon, Li-rich layered oxide cathodes for next-generation Li-ion batteries: chances and challenges, J. Electrochem. Soc. 162 (14) (2015) A2490.

[8] J. Song, B. Li, Y. Chen, Y. Zuo, F. Ning, H. Shang, G. Feng, N. Liu, C. Shen, X. Ai, D. Xia, A high-performance Li-Mn-O Li-rich cathode material with Rhombohedral symmetry via Intra layer Li/Mn disordering, Adv. Mater. 32 (16) (2020) 2000190.

[9] J.-M. Tarascon, Is lithium the new gold? Nat. Chem. 2 (2010) 510.

[10] E.A. Olivetti, G. Ceder, G.G. Gaustad, X. Fu, Lithium-ion battery supply chain considerations: analysis of potential bottlenecks in critical metals, Joule 1 (2017) 229–243.

[11] M. Armand, P. Axmann, D. Bresser, M. Copley, K. Edström, C. Ekberg, D. Guyomard, B. Lestriez, P. Novak, M. Petranikova, et al., Lithium-ion batteries – Current state of the art and anticipated developments, J. Power Sources 479 (2020) 228708.

[12] D. Bresser, K. Hosoi, D. Howell, H. Li, H. Zeisel, K. Amine, S. Passerini, Perspectives of automotive battery R&D in China, Germany, Japan, and the USA, J. Power Sources 382 (2018) 176–178.

[13] M. Marinaro, D. Bresser, E. Beyer, P. Faguy, K. Hosoi, H. Li, J. Sakovica, K. Amine, M. Wohlfahrt-Mehrens, S. Passerini, Bringing forward the development of battery cells for automotive applications: perspective of R&D activities in China, Japan, the EU and the USA, J. Power Sources 459 (2020) 228073.

[14] G.E. Blomgren, The development and future of lithium ion batteries, J. Electrochem. Soc. 164 (1) (2017): A5019–A5025.

[15] M. Bianchini, M. Roca-Ayats, P. Hartmann, T. Brezesinski, J. Janek, There and back again - the journey of LiNiO2 as cathode active material, Angew. Chem. Int. Ed. 58 (2019) 10434–10458.

[16] C. Vaalma, D. Buchholz, M. Weil, S. Passerini, A cost and resource analysis of sodium-ion batteries, Nat. Rev. Mater. 3 (2018) 18013.

[17] J.H. Kim, H.H. Ryu, S.J. Kim, C.S. Yoon, Y.-K. Sun, Degradation mechanism of highly Ni-rich Li[Ni$_x$Co$_y$Mn$_{1-x-y}$]O$_2$ cathodes with x > 0.9, ACS Appl. Mater. Interfaces 11 (2019) 30936–30942.

[18] M. Li, J. Lu, Z. Chen, K. Amine, 30 Years of lithium-ion batteries, Adv. Mater. 30 (33) (2018) 1800561.

[19] D. Bresser, D. Buchholz, A. Moretti, A. Varzi, S. Passerini, Alternative binders for sustainable electrochemical energy storage –the transition to aqueous electrode processing and bio-derived polymers, Energy Environ. Sci. 11 (2018) 3096–3127.

[20] L. Simonelli, A. Sorrentino, C. Marini, N. Ramanan, D. Heinis, W. Olszewski, A. Mullaliu, A. Birrozzi, N. Laszczynski, M. Giorgetti, S. Passerini, D. Tonti, Role of manganese in lithium- and ManganeseRich layered oxides cathodes, J. Phys. Chem. Lett. 10 (12) (2019) 3359–3368.

[21] D. Buchholz, J. Li, S. Passerini, G. Aquilanti, D. Wang, M. Giorgetti, X-ray absorption spectroscopy investigation of lithium- rich, cobalt-poor layered-oxide cathode material with high capacity, Chemelectrochem 2 (2015) 85.

[22] S. Ali, W. Olszewski, A. Sorrentino, C. Marini, A. Kazzazi, N. Laszczynski, A. Birrozzi, A. Mullaliu, S. Passerini, D. Tonti, L. Simonelli, Local interactions governing the performances of lithium- and manganese-rich cathodes, J. Phys. Chem. Lett. 12 (4) (2021) 1195–1201.

[23] U.-H. Kim, D.-W. Jun, K.-J. Park, Q. Zhang, P. Kaghazchi, D. Aurbach, C.M. Wang, D. Ahn, C.S. Yoon, Y.-K. Sun, et al., Pushing the limit of layered transition metal oxide cathodes for high-energy density rechargeable Li ion batteries, Energy Environ. Sci. 11 (2018) 1271–1279.

[24] L. de Biasi, B. Schwarz, T. Brezesinski, P. Hartmann, J. Janek, H. Ehrenberg, Chemical, structural, and electronic aspects of formation and degradation behavior on different length scales of Ni-rich NCM and Li-rich HE-NCM cathode materials in Li-ion batteries, Adv. Mater. 31 (2019) 1900985.

[25] E. Hu, X. Yu, R. Lin, X. Bi, J. Lu, S. Bak, K. Nam, H.L. Xin, C. Jaye, D.A. Fischer, et al., Evolution of redox couples in Li-and Mn-rich cathode materials and mitigation of voltage fade by reducing oxygen release, Nat. Energy 3 (2018) 690–698.

[26] M. Sathiya, A.M. Abakumov, D. Foix, G. Rousse, K. Ramesha, M. Saubanère, M. L. Doublet, H. Vezin, C.P. Laisa, A.S. Prakash, D. Gonbeau, G. VanTendeloo, J. M. Tarascon, Origin of voltage decay in high-capacity layered oxide electrodes, Nat. Mater. 14 (2015) 230.

[27] D. Eum, B. Kim, S.J. Kim, H. Hyeokjun Park, J. Wu, S. Cho, G. Yoon, M.H. Lee, S. Jung, W. Yang, W.M. Seong, K. Ku, O. Tamwattana, S.K. Park, I. Hwang, K. Kang, Voltage decay and redox asymmetry mitigation by reversible cation migration in lithium-rich layered oxide electrodes, Nat. Mater. 19 (2020) 419–427.

[28] W. Yin, A. Grimaud, G. Rousse, A.-M. Abakumov, A. Senyshyn, L. Zhang, S. Trabesinger, A. Iadecola, D. Foix, D. Giaume, J.M. Tarascon, Structural evolution at the oxidative and reductive limits in the first electrochemical cycle of Li$_{1.2}$Ni$_{0.13}$Mn$_{0.54}$Co$_{0.13}$O$_2$, Nat. Commun. 11 (2020) 1252.

[29] R.A. House, U. Maitra, M.A. Pérez-Osorio, J.G. Lozano, L. Jin, J.W. Somerville, L. C. Duda, A. Nag, A. Walters, K.-J. Zhou, et al., Superstructure control of first-cycle voltage hysteresis in oxygen-redox cathodes, Nature 577 (2020) 502–508.

[30] H. Liu, K.J. Harris, M. Jiang, Y. Wu, G.R. Goward, G.A. Botton, Unraveling the rapid performance decay of layered HighEnergy cathodes: from nanoscale degradation to drastic bulk evolution, ACS Nano 12 (2018) 2708–2718.

[31] T. Evans, D.M. Piper, H. Sun, T. Porcelli, S.C. Kim, S.S. Han, Y.S. Choi, C. Tian, D. Nordlund, M.M. Doeff, et al., In situ engineering of the Electrode– electrolyte interface for stabilized overlithiated cathodes, Adv. Mater. 29 (2017) 1604549.

[32] H. Lee, S.B. Lim, J.Y. Kim, M. Jeong, Y.J. Park, W.-S. Yoon, Characterization and control of irreversible reaction in Li-rich cathode during the initial charge process, ACS Appl. Mater. Interfaces 10 (2018) 10804–10818.

[33] K. Kleiner, B. Strehle, A.R. Baker, S.J. Day, C.C. Tang, I. Buchberger, F.-F. Chesneau, H.A. Gasteiger, M. Piana, Origin of high capacity and poor cycling stability of Li-rich layered oxides: a long-duration in situ synchrotron powder diffraction study, Chem. Mater. 30 (2018) 3656–3667.

[34] W. Hua, S. Wang, M. Knapp, S.J. Leake, A. Senyshyn, C. Richter, M. Yavuz, J. R. Binder, C.P. Grey, H. Ehrenberg, et al., Structural insights into the formation and voltage degradation of lithium- and manganese-rich layered oxides, Nat. Commun. 10 (2019) 5365.

[35] S. Muhammad, S. Lee, H. Kim, J. Yoon, D. Jang, J. Yoon, J.-H. Park, W.-S. Yoon, Deciphering the thermal behavior of lithium rich cathode material by in situ X-ray diffraction technique, J. Power Sources 285 (2015) 156–160.

[36] C. Genevois, H. Koga, L. Croguennec, M. Ménétrier, C. Delmas, F. Weill, Insight into the atomic structure of cycled lithium-rich layered oxide

Li1.20Mn0.54Co0.13Ni0.13O2 using HAADF STEM and electron nano-diffraction, J. Phys. Chem. C 119 (2015) 75–83.

[37] J.-G. Han, S.J. Lee, J. Lee, J.-S. Kim, K.T. Lee, N.-S. Choi, Tunable and robust phosphite-derived surface film to protect lithium-rich cathodes in lithium-ion batteries, ACS Appl. Mater. Interfaces 7 (2015) 8319–8329.

[38] Y. Yu, P. Karayaylali, D. Sokaras, L. Giordano, R. Kou, C.-J. Sun, F. Maglia, R. Jung, F.S. Gittleson, Y. Shao-Horn, Towards controlling the reversibility of anionic redox in transition metal oxides for high-energy Li-ion positive electrodes, Energy Environ. Sci. 14 (2021) 2322–2334.

[39] W. Olszewski, M.A. Perez, C. Marini, E. Paris, X. Wang, T. Iwao, M. Okubo, A. Yamada, T. Mizokawa, N.L. Saini, L. Simonelli, Temperature dependent local structure of Na_xCoO_2 cathode material for rechargeable sodium-ion batteries, J. Phys. Chem. C 120 (2016) 4227–4232.

[40] W. Olszewski, I. Isturiz, C. Marini, M. Avila, M. Okubo, H. Li, H. Zhou, T. Mizokawa, N.L. Saini, L. Simonelli, Phys. Chem. Chem. Phys. 20 (2018) 15288–15292.

[41] J. Li, R. Klèpsch, M.C. Stan, S. Nowak, M. Kunze, M. Winter, S. Passerini, Synthesis and electrochemical performance of the high voltage cathode material Li $[Li_{0.2}Mn_{0.56}Ni_{0.16}Co_{0.08}]O_2$ with improved rate capability, J. Power Sources 196 (2011) 4821–4825.

[42] A. Kazzazi, D. Bresser, A. Birrozzi, J. Von Zamory, M. Hekmatfar, S. Passerini, Comparative analysis of aqueous binders for high-energy Li-rich NMC as a lithium-ion cathode and the impact of adding phosphoric acid, ACS Appl. Mater. Interfaces 10 (2018) 17214–17222.

[43] L. Simonelli, C. Marini, W. Olszewski, M. Ávila Pérez, N. Ramanan, G. Guilera, V. Cuartero, K. Klementiev, CLÆSS: the hard X-ray absorption beamline of the ALBA CELLS synchrotron, Cogent Phys. 3 (2016) 1231987.

[44] B. Ravel, M. Athena Newville, Hephaestus Artemis, Data analysis for X-ray absorption spectroscopy using IFEFFIT, J. Synchrotron Radiat. 12 (2005) 537–541.

[45] R. Prins, D.C. Koningsberger (Eds.), X-Ray Absorption: Principles, Applications, Techniques of EXAFS, SEXAFS, XANES, Wiley, New York, 1988.

[46] G. Vanko, T. Neisius, G. Molnar, F. Renz, S. Karpati, A. Shukla, F.M.F. de Groot, Probing the 3d spin momentum with X-ray emission spectroscopy: the case of molecular-spin transitions, J. Phys. Chem. B 110 (2006) 11647–11653.

[47] Z. Huang, F. Du, C. Wang, D. Wang, G. Chen, Low-spin Mn^{3+} ion in rhombohedral $LiMnO_2$ predicted by first-principles calculations, Phys. Rev. B Condens. Matter 75 (2007): 054411.

[48] A.A. Guda, N. Smolentsev, M. Rovezzi, E.M. Kaidashev, V.E. Kaydashev, A. N. Kravtsova, V.L. Mazalova, A.P. Chaynikov, E. Weschke, P. Glatzel, A. V. Soldatov, Spin-polarized electronic structure of the Core−Shell ZnO/ZnO: Mn nanowires probed by Xray absorption and emission spectroscopy, J. Anal. At. Spectrom. 28 (2013) 1629.

[49] K. Yang, D.I. Khomskii, H. Wu, Unusual layered order and charge disproportionation in the double-perovskite compound Ca_2FeMnO_6, Phys. Rev. B Condens. Matter 98 (2018): 085105.

[50] H. Wu, T. Burnus, Z. Hu, C. Martin, A. Maignan, J.C. Cezar, A. Tanaka, N. B. Brookes, D.I. Khomskii, L.H. Tjeng, Ising magnetism and ferroelectricity in Ca3CoMnO6, Phys. Rev. Lett. 2 (2009): 026404.

[51] G. Amatucci, A. Du Pasquier, A. Blyr, T. Zheng, J.-M. Tarascon, The elevated temperature performance of the LiMn2O4/C system: failure and solutions, Electrochim. Acta 45 (1999) 255.

[52] S. Demirel, E. Oz, S. Altin, A. Bayri, E. Altin, S. Avci, Enhancement of battery performance of LiMn2O4: correlations between electrochemical and magnetic properties, RSC Adv. 6 (2016) 43823.

[53] S.K. Mishra, G. Ceder, Structural stability of lithium manganese oxides, Phys. Rev. B Condens. Matter 59 (1999) 6120.

[54] P. Glatzel, U. Bergmann, High resolution 1s core hole X-ray spectroscopy in 3d transition metal complexes-electronic and structural information, Coord. Chem. Rev. 249 (2005) 65.

[55] N. Laszczynski, J. von Zamory, J. Kalhoff, N. Loeffler, V.S.K. Chakravadhanula, S. Passerini, Improved performance of VOx-coated Li-rich NMC electrodes, Chemelectrochem 2 (2015) 1768.